International Journal of Heat and Mass Transfer 130 (2019) 1108–1119

Contents lists available at ScienceDirect

International Journal of Heat and Mass Transfer

journal homepage: www.elsevier.com/locate/ijhmt

Embedded cooling with 3D manifold for vehicle power electronics application: Single-phase thermal-fluid performance

Ki Wook Jung [a], Chirag R. Kharangate [b], Hyoungsoon Lee [c], James Palko [d], Feng Zhou [e], Mehdi Asheghi [a], Ercan M. Dede [e], Kenneth E. Goodson [a,*]

[a] Mechanical Engineering Department, Stanford University, Stanford, CA 94305, United States
[b] Mechanical and Aerospace Engineering Department, Case Western Reserve University, Cleveland, OH 44106, United States
[c] School of Mechanical Engineering, Chung-Ang University, Seoul, 06974, South Korea
[d] University of California, Merced, Merced, CA 95343, United States
[e] Toyota Research Institute of North America, Ann Arbor, MI 48105, United States

ARTICLE INFO

Article history:
Received 20 June 2018
Received in revised form 20 October 2018
Accepted 25 October 2018
Available online 13 November 2018

Keywords:
Embedded microchannel
3D manifold
Monolithic microcooler
Conjugate thermal-fluidic numerical simulations
Single-phase water cooling experiments

ABSTRACT

Single-phase thermal-fluidic performance of an embedded silicon microchannel cold-plate (25 parallel channels: 75 μm × 150 μm) with a 3-D liquid distribution manifold (6 inlets: 700 μm × 150 μm) and vapor extraction conduits, is investigated using water as working fluid. A 3D manifold is fabricated from silicon and bonded to a silicon microchannel substrate to form a monolithic microcooler (μ-cooler). A metal serpentine bridge (5^2 mm^2 of footprint) and multiple resistance temperature detectors (RTDs) are used for electrical Joule-heating and thermometry, respectively. The experimental results for maximum and average temperatures of the chip, pressure drop, thermal resistance (as low as 0.68 K/W), average heat transfer coefficient (~30,000–50,000 W/m^2 K) for flow rates of 0.03, 0.06 and 0.1 l/min and heat fluxes of 60, 100 and 250 W/cm^2 are reported. The embedded microchannel-3D manifold μ-cooler device is capable of removing 250 W/cm^2 at a maximum temperature of 90 °C with less than 3 kPa pressure drop for a flow rate of 0.1 l/min. The results from conjugate thermal-fluidic numerical simulations agree well with the experimental data over the wide range of heat fluxes and flow conditions. The numerical simulation results also hint at the possibility of removing up to ~850 W/cm^2 using single-phase water at a maximum temperature of 166 °C at the same pressure drop and flow rate. This offers a very attractive strategy/option for cooling of high heat flux power electronics using single-phase water.

1. Introduction

Wide-spread utilization of hybrid electric vehicles is strongly dependent on designing components that not only have higher weight-to-volume ratios but are also economical to manufacture [1]. To achieve this goal, new and improved thermal control strategies must be implemented that reduce weight and volume while improving cooling efficiency. Traditional heat sink designs utilize indirect (remote) cooling schemes, where the liquid is passed through a heat sink with a thermal interface material sandwiched between the heat sink and semiconductor device. The total thermal resistance is a summation of conduction resistance components of each solid layer, an advection resistance component due to absorbed energy to the coolant through the heat exchanger, and a convection resistance component of the fluid flow in the heat sink. Utilizing direct cooling or an "embedded cooling" strategy can eliminate most of these resistances as it directly cools the semiconductor device closest to the heat source [2]. Tuckerman and Pease also pointed out that the convection resistance component is dominant over the other components, and specifically, the conduction resistance component can be significantly reduced by thinning substrate thickness for intimate thermal contact with the heat exchanger [3]. As suggested by others, embedded cooling strategies eliminate the majority of conduction thermal resistances, but the effect on convective component depends on the working fluid and the heat sink design and geometry as well as liquid delivery and distribution scheme and configuration. Direct cooling strategies also might have a limitation in terms of embedded cooling channel heights due to the confined substrate thickness of heat sink. As a result, the smaller channel height has a higher pressure drop requirement, which leads to increased pumping power of the system.

* Corresponding author.
E-mail address: goodson@stanford.edu (K.E. Goodson).

https://doi.org/10.1016/j.ijheatmasstransfer.2018.10.108
0017-9310/© 2018 Published by Elsevier Ltd.

Nomenclature

A_{wet}	the wetted heat transfer area between water and microchannels in the cold plate
f_1, f_2	the scaling factors representing the ratios between $T_{heater,avg\text{-}local}$ to $T_{heater,avg\text{-}global}$, $T_{heater,max}$, respectively from the CFD simulations
G	mass flux, [kg/m^2-s]
h	the heat transfer coefficient, [kW/m^2 K]
H	height of microchannels, [μm]
$K_{contraction}$	the gradual contraction coefficient between a manifold inlet plenum and a manifold inlet conduit
ΔP	pressure drop, [kPa]
δ_{base}	substrate base thickness, [μm]
Q	mass or volume flow rate, [g/min] or [l/min]
q_{heater}	supplied heat through the heater, [W]
q_{trans}	net heat transmitted to the fluid, [W]
q_{loss}	heat loss, ($=q_{heater} - q_{trans}$), [W]
q''	supplied heat flux through heater, [W/cm^2]
R	thermal resistance, [°C/W]
T	temperature, [°C]
U	uncertainty of thermal-fluidic parameters
W	width of microchannels, [μm]

Subscripts

advection	fluid advection
avg	average
ch,base	microchannel base in the cold plate
cp	cold plate
exp	experimental
fl	fluid
fin	microchannel wall between two adjacent microchannels in the cold plate
in/out	inlet/outlet
max	maximum
mani	manifold
plen	manifold inlet plenum
CFD	predicted value from CFD simulation
sat	saturation
wall	microchannel wall between inlet and outlet conduits in the manifold

To address this challenge, researchers have adopted innovative 3D manifolding architectures (e.g. Forced-fed Microchannel Heat Sinks or FFMHS) which provide low thermal resistance without increasing the pressure drop across the heat sink [4–20].

Early numerical modeling in the topic of 3D manifold liquid delivery configuration was performed by Harpole and Eninger [4] who predicted heat transfer coefficients on the order of 100,000 W/m^2 K. Ryu et al. [5] numerical simulation results indicated that an optimized manifold design reduced the thermal resistance by 50% compared to a traditional microchannel heat sink. In another study, Kim et al. [6] showed a 35% reduction compared to a traditional heat sink design in thermal resistance utilizing an informed manifold design. An experimental work by Kermani et al. [7] showed manifold architecture can provide a heat transfer coefficient as high as 65,480 W/m^2 K with a flow rate of 1.1 g/s using water.

A numerical study by Boteler et al. [8] indicated a more uniform flow distribution and lower pressure drop by as much as 97% for a 3D manifold design compared to a traditional microchannel design. Recently, Arie et al. [9–11] conducted manifold design optimization (unit cell) that resulted in both reducing the thermal resistance and reducing the pumping power requirements. Sarangi et al. [12] examined the impact of manufacturing tolerances on optimization of manifold microchannel heat sinks. Zhou et al. [13] further studied a manifold mini/microchannel heat sink with a highly modular and reconfigurable manifold for custom flow solutions and performance in power electronics cooling applications.

Recently, many researchers have achieved the maximum removable heat fluxes in excess of 1 kW/cm^2 [14–20] and one common condition in these systems is phase-change or two-phase convective heat transfer in multi-layered 3D manifolding heat exchangers because of excellent cooling efficiency as well as reduced pumping power.

Cetegen [14] demonstrated that FFMHS technology that utilizes alternate inlet and outlet channels reduces the pressure drop in singe-phase flows because of a lower flow rate requirement and shorter fluid flow path while still maintaining a high heat transfer coefficient due to the thermally developing nature of flow in the microchannels. The optimized FFMHS could achieve 72% and 306% more heat transfer compared to Traditional Microchannel Heat Sinks, or TMHS, and Jet Impingement Heat Sinks, or JIHS, respectively for constant pumping power condition. A maximum removable heat flux of the FFMHS was reported as 1.23 kW/cm^2 with the total pressure drop of 60.3 kPa [14].

Bae et al. [16] and Mandel et al. [17] introduced a thin-Film Evaporation and Enhanced fluid Delivery System, or FEEDS, which also had alternated inlet and outlet channels attached to cooling microchannels of the heat sink. The reported maximum removable heat flux was 1 kW/cm^2 with total pressure drop up to 90 kPa, and a vapor quality of 45%, which effectively reduced significant amount of energy spent on subcooling or pumping power [17].

Drummond et al. [18,19] also developed intrachip heat sink systems that consist of multi-layer hierarchical manifolds, and demonstrated the effects of cooling channel dimensions and mass flux on the maximum heat flux dissipation [18] and the heat transfer coefficient [19] while uniform background heat fluxes with simultaneous hotspot heating were applied. They have reported that uniform background heat fluxes up to 0.5 and 1.02 kW/cm^2 were dissipated while the system pressure drop were up to 50 and 120 kPa, respectively [18,19]. However, the two-phase cooling systems described above still reported significant amount of the total pressure drop that is closely related to the increased pumping power of the heat exchangers. Therefore, we have focused on further design optimization of embedded microchannel with 3D manifold cooling system to achieve the decreased pumping power along with the excellent heat transfer performance.

Recently, Jung et al. [20] conducted a parametric study and investigated thermal design considerations and constraints for development of an embedded silicon/SiC microchannel cooling with 3D manifold architecture capable of removing up to 1 kW/cm^2 by means of single/two-phase flow and heat transfer schemes. They implemented analytical microchannel correlations and a control volume based approach to predict thermal resistance and pressure drop in microchannels with connectional (2D) linear and 3D manifolding architectures. It was shown that for a given thermal resistance, the 3D manifold architecture pressure drop is an order of magnitude lower that of a 2D linear-manifold. While the Jung et al. [15] study provided general preliminary design guidelines for microchannel and 3D manifold geometry and configuration, the uncertainty in the correlations demanded a follow up experimental investigation.

In the present experimental study, we measured the thermal resistance and pressure drop characteristics and thermofluidic performance of a microfabricated embedded silicon microchannel with 3D manifold micro-conduit liquid delivery system. DI water was used as the working fluid and fluid flow rates between 0.033 l/min and 0.104 l/min were tested with applied heat fluxes of 59.93–251.71 W/cm^2. At the flow rate of 0.104 l/min and the heat flux of 251.74 W/cm^2, we could achieve a notably low total system pressure drop of 2.36 kPa and total thermal resistance of 0.58 °C/W.

2. Experimental method

2.1. Design and microfabrication of embedded microchannels with 3-D manifold μ-cooler

Fig. 1(a) describes the conceptual design and working principle of the in-chip cooler. A cold plate with etched microchannels is bonded to a 3-D manifold with etched fluid inlet and outlet micro-conduits. Coolant, deionized (DI) water, is flowing through multiple inlet micro-conduits of the manifold ( ), and the fluid is divided into two streams at the intersections between the manifold inlet micro-conduits and the cold plate microchannels that are perpendicular to the direction to the manifold micro-conduits. This flow arrangement results in direct impingement of the flow to the bottom of the heated section of the cold-plate microchannel, exchanging heat with the walls and the base of the microchannels ( ) followed by a 180° U-turn to exit through the adjacent outlet micro-conduits of the manifold ( ).

Uniform heat fluxes, from 60 to 250 W/cm^2, were applied at the top surface of the cold-plate by means of electrical Joule-heating in a serpentine Ti/Au heater covering a 5 × 5 mm^2 active region of the cold plate. The top surface temperature is monitored at several locations using RTDs placed in between the serpentine heater lines. The RTDs are located diagonally to provide a clear picture of the heating and flow patterns, depicted in Fig. 2(a). The RTDs were calibrated individually before every measurement, the temperature coefficient of resistant (TCR) of the RTDs ranged from 0.00167 to 0.00173/°C and the change of TCR was maintained within 0.7% after each experiment. We could only utilize 5 out of a total 14 RTDs (RTD5, 6, 7, and 9: highlighted in Fig. 2a) due to microfabrication defects. The RTD located at the center of the chip was not functional, as a result the heater maximum temperature, $T_{heater,max}$ is calculated by taking the average temperature of the RTDs 5, 6, 7, and 9, in combination with the scaling factor calculated from the CFD modeling, the process is detailed in Section 3.2.1. The associated uncertainty with this procedure is quantified in Section 3.2.1 and is estimated to be 1.4–3.1%.

Two silicon substrates were prepared for the cold plate and manifold layers. Using standard microfabrication techniques, alignment marks were defined and isotropically etched on front and backside of both substrates (Fig. 3, Step 1). In the cold plate, microchannels for convective cooling were anisotropically etched from the backside. In the manifold, there were two anisotropic etch processes to define the microstructures. The 3D manifold fluid inlet and exit micro-conduits, inlet plenums, pressure taps and flow distributors were etched from the front side. After then, thin Al layer was sputtered to protect the etched features from the front side and holes for fluid inlet supply, and exit micro-conduits were etched from the backside until they were etched through (Fig. 3, Step 2).

Fig. 2(b) shows the location of each structure and identifies key dimensions of each feature in the cold plate and the manifold. In addition, all of the dimensions of the defined structures from Step 2 are listed in Table 1. After all of the microstructures in each substrate were defined, the manifold substrate was cleaned in Al etchant to remove residual Al on the surface and it went through organic cleaning in a Piranha bath. Since there had been no metal on the cold plate substrate, the cold plate substrate was cleaned in a Piranha bath only. Ti/Au eutectic bond layers were deposited on bond interfaces, bottom surface of the cold plate and top surface of the manifold, by a metal evaporation process. Another organic clean process was conducted after the metal evaporation process, and both substrates were aligned with the predefined bonding alignment marks from Step 1. Au-Si eutectic bond was formed while high process temperature, 410–420 °C, and high compressive pressure, >425 kPa, conditions were applied to the bond interfaces (Fig. 3, Step 3). Lastly, PECVD SiO_2 and Ti/Au layers were deposited on the top surface of the bonded substrate to define an electrical insulation layer, and a metal serpentine heater and RTDs, respectively.

2.2. Test module

A polycarbonate plastic (Lexan) test module is manufactured, see Fig. 4, that contains A Lexan block two inlet ports on the side walls and one outlet port on the bottom wall. The microfabricated sample is placed on the top side of the test module where the inlet

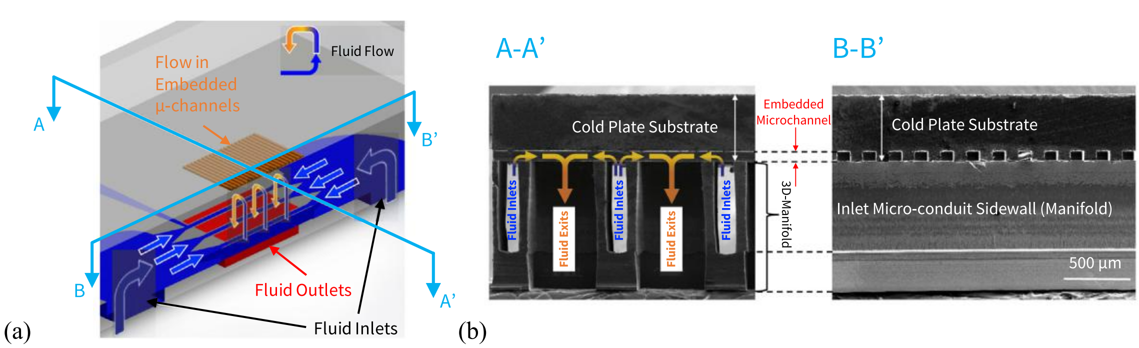

Fig. 1. (a) Conceptual design of an in-chip scale embedded microchannel-3D manifold cooler: the blue arrow ( ) depicts fluid flow and distribution of cold liquid through multiple inlet micro-conduits, followed by a 90° turn to enter the cold plate microchannels, exchanging heat in a direct impingement flow configuration (: color code depicts the fluid heating up), followed by an 180° U-turn to exit through the adjacent outlet micro-conduits of the manifold (: color code depicts the fluid heated up); also see the top-left inset for flow and heat exchange pattern. (b) cross-sectional views of embedded microchannels and manifold inlet/exit channels. (A-A′) shows the direction of fluid flow from the manifold to the cold plate, and back to the manifold. The fluid is introduced to the manifold inlet micro-conduits ( ), transverses the cold-plate embedded microchannels ( ), and moves out the embedded microchannels to the manifold exit micro-conduits ( ). (B-B′) shows the array of embedded microchannels in the cold plate and one of the inlet channels in the manifold. (For interpretation of the references to color in this figure legend, the reader is referred to the web version of this article.)

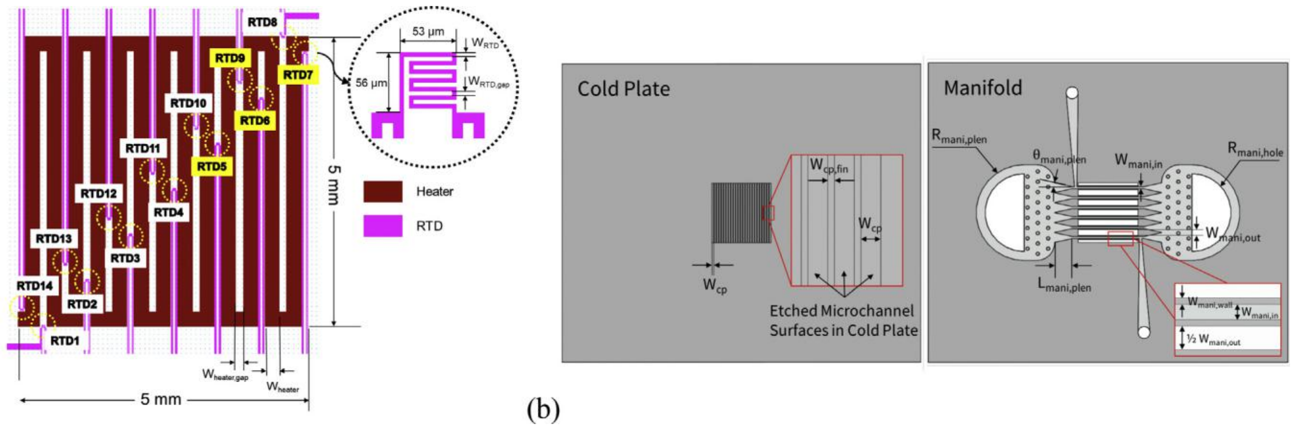

Fig. 2. (a) A Ti/Au serpentine heater with RTDs are placed on a 5 × 5 mm^2 center area of the cold plate. RTDs are diagonally placed in between the heater lines and only RTD5, 6, 7, and 9 (highlighted) were used for actual temperature measurement. Measured temperature coefficient of resistance (TCR) of RTDs was 1.4–1.8 × 10^{-3} °C^{-1} and the thicknesses of the heater and the RTD are 500 nm, and 50–55 nm, respectively. A closed-loop flow system is used for RTD calibration by varying the temperature of the liquid and recording corresponding electrical resistance for individual RTDs. (b) Design of various anisotropically etched structures in the cold plate and the manifold, see Table 1 for geometry details. A set of pin fin arrays at the entrance and exit plenums are utilized to create uniform flow distribution. As the inlet plenums and inlet micro-conduits are interconnected, these features were protected by a thin Al layer while exit micro-conduits and holes for fluid inlet supply were etched from the backside.

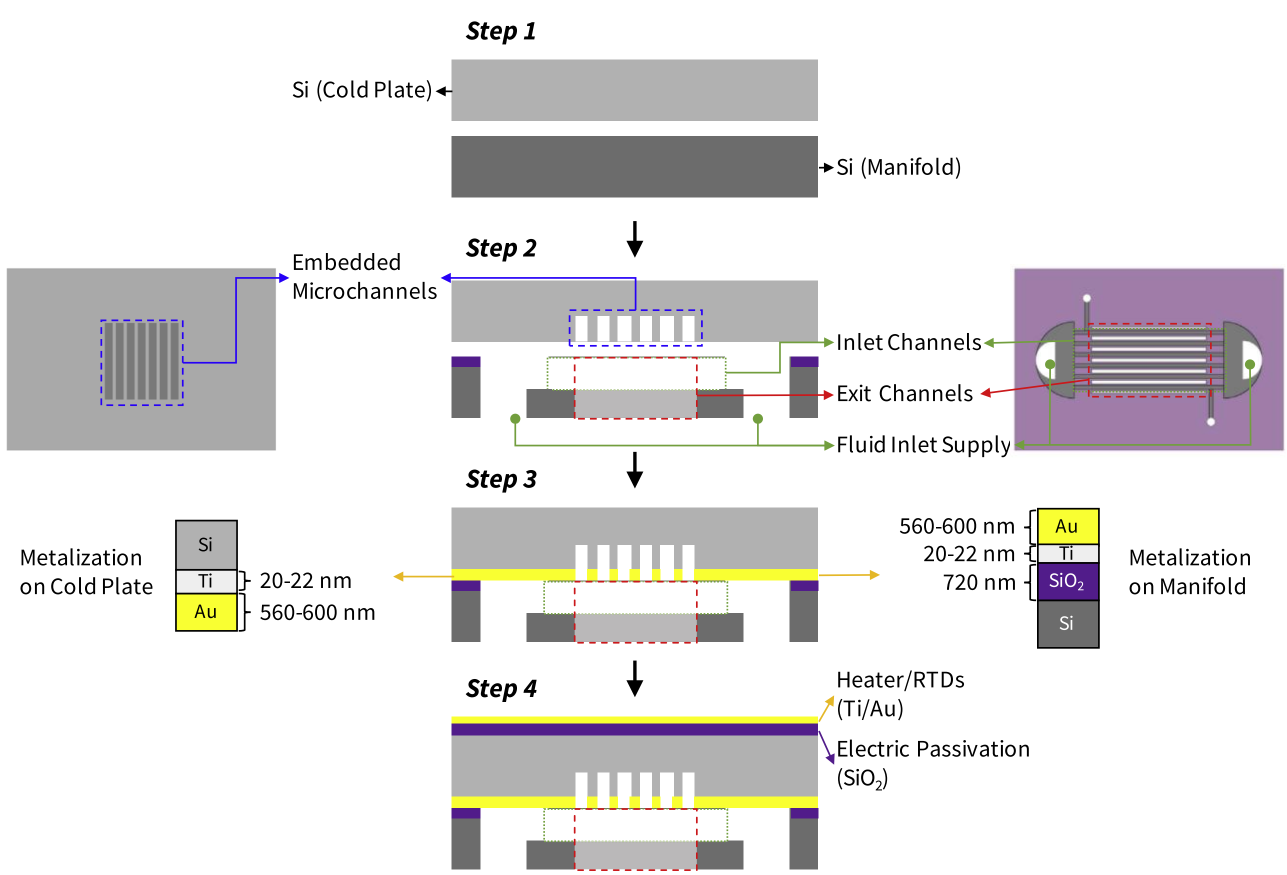

Fig. 3. Overall microfabrication process of the embedded microchannel-3D manifold cooler. *Step 1*: double-polished Si substrates with thickness of 500 μm, and 1000 μm were prepared for the cold plate and the 3D manifold structures, respectively. *Step 2*: Microchannels and other microscale features were anisotropically etched in the cold plate and the 3D manifold substrates. Double-sided anisotropic Si etch technique was used to define the microstructures with different etch depth in the 3D manifold. *Step 3*: Au-Si eutectic bond layers were deposited on the cold plate and the 3D manifold substrates. Ti/Au layer thickness on each substrate is denoted in Fig. 2. As the Ti layer on the cold plate functioned as a native oxide getter, Au-Si eutectic reaction was activated from the cold plate surface. 720 nm of SiO_2 layer on the manifold substrate insulated Si from the Au layer and it helps to induce better Au-Si eutectic reaction [22]. *Step 4*: A serpentine heater and RTDs were deposited on top of Si_xN_y/SiO_2 electric passivation layer. Since Ti reacts with SiO_2 at high temperatures, it is recommended to deposit a thin Si_xN_y layer between Ti and SiO_2 layers to prevent further reaction.

and outlet openings on the sample and the module mate with each other. Fluid pressure is measured at the inlet and outlet of the test module with ports milled into the test module. Fluid temperature measurements are made with type-K thermocouples, having ±1 °C error, inserted into the flow in separate inlet and outlet ports.

2.3. Flow loop system

A fluid flow loop, depicted in Fig. 5, is used to achieve the desired test conditions at the inlet of the test module. Water is used as the working fluid for the current experiments. A magneti-

Table 1
Dimensions of structures in the cold plate and the 3-D manifold determined through prior studies in [15].

Substrates	Structures	Symbols	Dimensions
Cold plate	Microchannels	H_{cp}	75 μm
		W_{cp}	150 μm
		$W_{cp,fin}$	50 μm
	Serpentine heater	W_{heater}	250 μm
		$W_{heater,gap}$	125 μm
	RTD	W_{RTD}	4 μm
		$W_{RTD,gap}$	4 μm
Manifold	Inlet micro-conduits	$H_{mani,in}$	700 μm
		$W_{mani,in}$	150 μm
		$W_{mani,wall}$	81 μm
	Exit micro-conduits	$H_{mani,out}$	1000 μm
		$W_{mani,out}$	520 μm
	Inlet plenums	$R_{mani,plen}$	4 mm
		$L_{mani,plen}$	1.45 mm
		$\theta_{mani,plen}$	12.5°
	Fluid inlet supply	$R_{mani,hole}$	3.25 mm

cally coupled gear pump is used to pump the fluid from the reservoir to the test section and back. Exiting the pump, the fluid is passed through a Coriolis flow meter before entering a filter placed upstream of the test module. Exiting the test module, the heated fluid again passed through a filter and then a water-cooled liquid-to-liquid heat exchanger, which decreases the liquid temperature to ambient conditions before entering the reservoir.

2.4. Operating conditions, operating procedure, and measurement uncertainty

The operating conditions for the study were as follows: (1) Water inlet pressure, P_{in}, ranging from 146.60 to 246.75 kPa, (2) inlet temperature, T_{in}, ranging from 24.56 to 25.27 °C, and (3) mass flow rate, Q_{mass}, ranging from 32.50 to 103.51 g/min. The water inlet pressure was above atmospheric pressure at all time for two reasons: (i) supplying water from the reservoir to the flow loop always pressurizes the loop, and (ii) more pressure head is produced by the pump to circulate the fluid. Once the test section was integrated to the closed-loop flow system, LabVIEW code was utilized to control the micro-pump and to record temperature and pressure information related to both the fluid and the test sample. All measurements were taken once the system reached steady-state in the experiments. The thermocouples were placed near the fluid inlet and outlet plenums of the sample. Inlet pressure was measured at the inlet of the upstream preheater with an absolute pressure transducer and relative pressure difference was measured between the inlet and outlet plenums. The instrument accuracy information of each component is listed in Table 2.

3. Theoretical analysis

3.1. Data reduction

Electrical power is supplied through the serpentine heater, q_{heater}, which is multiplication of the supplied voltage and current in the power supply. Since single-phase water was used during the entire experiments, the net power that is transmitted to the working fluid, q_{trans}, can be estimated by measuring the change in sensible heat of the working fluid:

$$q_{trans} = q_{heater} - q_{loss} = \dot{m} \cdot \int_{T_{fl,in}}^{T_{fl,out}} C_p(T)dT \tag{1}$$

C_p is the saturated specific heat of single-phase water and we considered temperature-dependency in C_p. The heat loss, q_{loss}, is simply deducted by subtracting q_{trans} from q_{heater}.

The cooling performance of the μ-cooler is best described by the maximum total thermal resistance [15], $R_{total\text{-}max}$, which yields a conservative estimate of μ-cooler's thermal resistance. In addition, the contribution of the advection term, arising from the increase in the average temperature of the working fluid as it transverses along the heated section microchannels, is calculated by writing an energy balance for the water:

$$R_{total-max} = \frac{T_{heater,max} - T_{fl,in}}{q_{trans}} = \frac{\Delta T_{total}}{q_{trans}} \tag{2a}$$

$$R_{advection} = \frac{T_{fl,out} - T_{fl,in}}{q_{trans}} = \frac{\Delta T_{fl}}{q_{trans}} \tag{2b}$$

The convection thermal resistance, $R_{convection}$ can be estimated by $R_{convection} = R_{total-max} - R_{advection}$.

The heat transfer coefficient (HTC) of the device, h_{wall}, is a convective heat transfer rate at silicon microchannel walls and it is estimated by

$$h_{wall} = \frac{q_{trans}}{\eta_o \cdot (T_{base,avg} - T_{fl,ref}) \cdot A_{wet}} \tag{3a}$$

where η_o is overall fin efficiency, $T_{base,avg}$ is the average channel base temperature which is deducted from conduction resistance across the cold plate base layer, $T_{fl,ref}$ is the estimated average fluid temperature between inlet and outlet, and A_{wet} is channel wetted area. Each parameter is defined as:

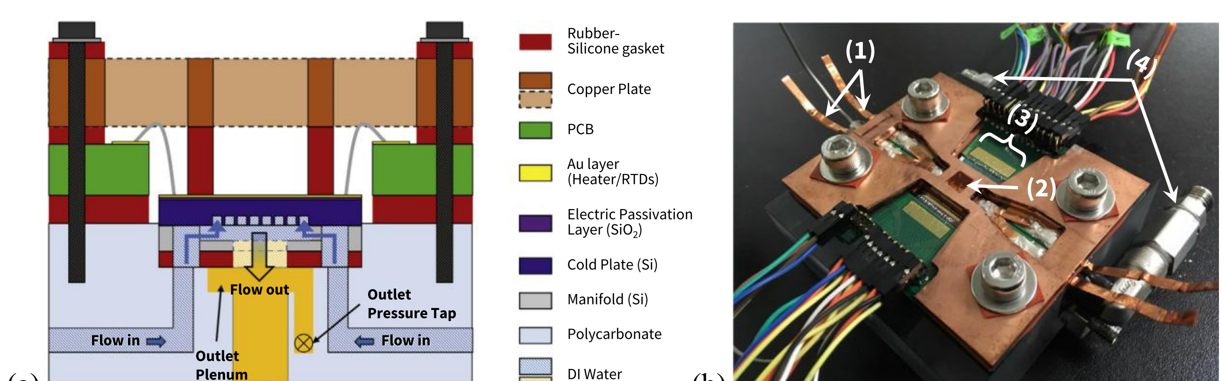

Fig. 4. (a) A cross-sectional view of an assembled test section, and (b) an image of the assembled test section. (1) Power supply lines, (2) 5 mm-by-5 mm heated region in the sample, (3) Au electrode pads that are connected to RTDs, (4) Swagelok fittings for inlet and exit pressure read-outs.

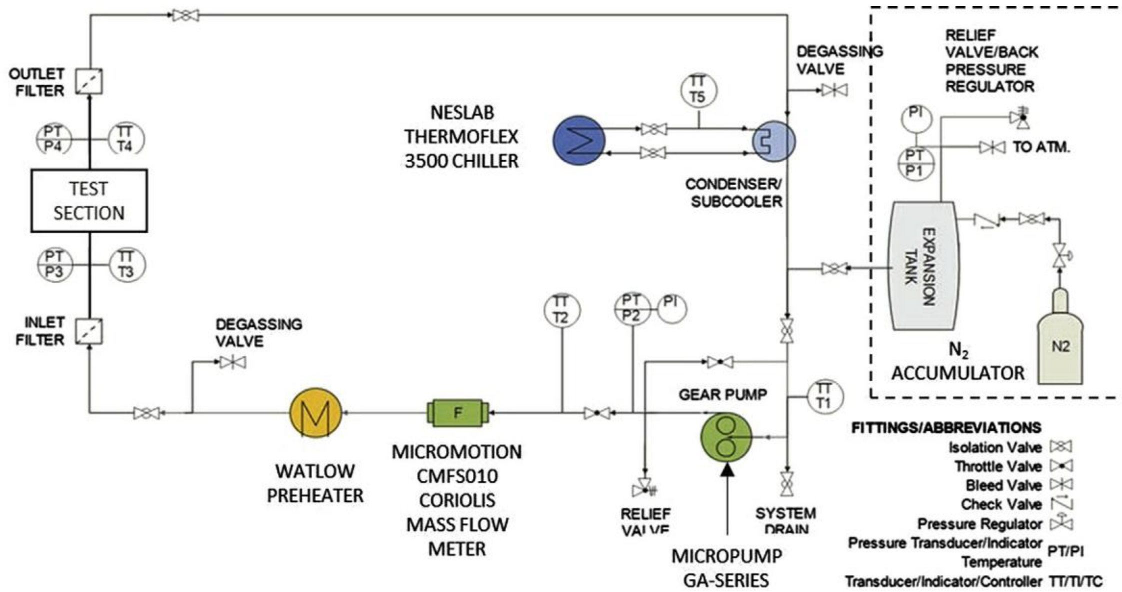

Fig. 5. Configuration of a closed-loop flow system for the experiments. Key components of the flow loop system are a micropump, a preheater after the pump, a preheater, a condenser, and an accumulator to allow setting the low pressure point in the flow loop. However, the accumulator was not used for the current experiments.

Table 2
A list of experimental tools in the test system and their accuracy information.

Experimental tools	Affected parameters	Accuracy
Thermocouple (K-type)[†]	$T_{fl,in}$, $T_{fl,out}$	±1 °C
Ti/Au RTD	$T_{heater,avg}$, $T_{heater,max}$	±1 °C
Micro Motion CMFS010 Coriolis mass flow meter	Q_{mass}	±0.10% of rate (Liquid)
NESLAB Thermoflex 3500 chiller	$T_{fl,in}$	±0.1 °C
Omega PX2300-5DI	ΔP_{total}	±0.25% RSS FS (FS: 0–5 psi)

[†] K-type thermocouples were individually calibrated to accuracy of <±0.5 °C, however, larger uncertainty level is considered in this study to stay on the conservative side.

$$T_{base,avg} = T_{heater,avg} - \frac{q_{trans} \cdot \delta_{base}}{k_{Si} \cdot A_{effect}} \tag{3b}$$

$$T_{fl,ref} = \frac{T_{fl,in} + T_{fl,out}}{2} \tag{3c}$$

$$\eta_o = 1 - \frac{N \cdot A_f}{A_{wet}} \cdot (1 - \eta_f) \tag{3d}$$

where N is the number of microchannels in the cold plate and η_f is the fin efficiency defined as:

$$\eta_f = \frac{\tanh(m \cdot H_{cp})}{m \cdot H_{cp}}, m = \sqrt{\frac{2 \cdot h_{wall}}{k_{Si} \cdot W_{cp,fin}}} \tag{3e}$$

The h_{wall} is first calculated by assuming the fin efficiency of unity in Eq. (3-d). After that, the fin efficiency was iterated until the h_{wall} was converged.

The total pressure drop, $\Delta P_{total,exp}$, in the μ-cooler with 3-D manifold is expressed as:

$$\Delta P_{total,exp} = \Delta P_{plenum} + \Delta P_{contraction} + \Delta P_{friction} + \Delta P_{expansion} \tag{4a}$$

where ΔP_{plenum} is the pressure drop in the inlet plenums, $\Delta P_{contraction}$ is the gradual contraction pressure losses from the inlet plenum to the manifold inlet conduits, $\Delta P_{friction}$ is the pressure drop due to frictional pressure losses across the microchannels, and $\Delta P_{expansion}$ is the expansion pressure losses from the microchannels to the manifold exit conduits.

$$\Delta P_{contraction} = K_{contraction} \cdot \frac{\rho_{in}}{2} \cdot v_{mani,in} \tag{4b}$$

$$\Delta P_{friction} = \frac{2L_{ch}}{D_h} \cdot f_f \cdot G^2 \cdot v_f \tag{4c}$$

where $K_{contraction}$ is the gradual contraction coefficient between a manifold inlet plenum and a manifold inlet conduit, $v_{mani,in}$ is the net liquid velocity at the beginning of a manifold inlet conduit, L_{ch} is the flow channel length, D_h is hydraulic diameter of the flow channel, f_f is friction factor of water, G is mass flux in the flow channel, and v_f is saturated liquid specific volume of water.

3.2. Uncertainty study

Here we carefully investigate the uncertainty [24] in the experimental data for surface temperature measured using RTDs (Section 3.2.1), thermal resistance and heat transfer coefficient (Section 3.2.2) as well as pressure drop (Section 3.2.3).

3.2.1. Uncertainty in measured surface temperature information, $T_{heater,max}$ and $T_{heater,avg}$

As noted in Section 2.1, due to microfabrication defects only four RTD5, 6, 7, and 9 were functional (located at upper-right area of the heater, see Fig. 2a). Therefore, the calculated average surface temperature using these four RTDs, $T_{heater,avg\text{-}local}$, is not a precise representation of the average temperature over the entire surface of the heater, $T_{heater,avg\text{-}global}$. The scaling factors $\boldsymbol{f_1}$ and $\boldsymbol{f_2}$, are calculated using CFD simulations, represent the ratios between $T_{heater,avg\text{-}local}$ to $T_{heater,avg\text{-}global}$, $T_{heater,max}$, respectively (see Table A.II.2). The associated uncertainty of $T_{heater,avg\text{-}global}$, and $T_{heater,max}$ are estimated to 1.4–3.1% considering ±1 °C uncertainty of the K-type thermocouple to measure $T_{fl,in}$ and $T_{fl,out}$ (Table 2).

3.2.2. Uncertainty in thermal resistance and heat transfer coefficient

The uncertainties in $R_{total\text{-}max}$, or $U_{R_{total-max}}$, and in $R_{advection}$, or $U_{R_{advection}}$, are given by [24]:

$$\left(\frac{U_{R_{total-max}}}{R_{total-max}}\right)^2 = \left(\frac{U_{T_{heater,max}}}{T_{heater,max} - T_{fl,in}}\right)^2 + \left(\frac{U_{T_{fl,in}}}{T_{heater,max} - T_{fl,in}}\right)^2 + \left(\frac{U_{q_{trans}}}{q_{trans}}\right)^2 \quad (5a)$$

$$\left(\frac{U_{R_{advection}}}{R_{advection}}\right)^2 = \left(\frac{U_{T_{fl,out}}}{T_{fl,out} - T_{fl,in}}\right)^2 + \left(\frac{U_{T_{fl,in}}}{T_{fl,out} - T_{fl,in}}\right)^2 + \left(\frac{U_{q_{trans}}}{q_{trans}}\right)^2 \quad (5b)$$

$$\left(\frac{U_{q_{trans}}}{q_{transfer}}\right)^2 = \left(\frac{1}{q_{trans}} \cdot \frac{dq_{trans}}{dT_{fl,in}} \cdot U_{T_{fl,in}}\right)^2 + \left(\frac{1}{q_{trans}} \cdot \frac{dq_{trans}}{dT_{fl,out}} \cdot U_{T_{fl,out}}\right)^2 \quad (5c)$$

where q_{trans} is the heat dissipation in the serpentine heater that is transferred to the liquid. The experimental uncertainties of q_{trans}, $T_{heater,max}$, $T_{fl,in}$, $T_{fl,out}$ are 6.4–63.0%, < 3%, ± 1 °C, and ± 1 °C, respectively. As a result, $U_{R_{total-max,exp}}$, $U_{R_{advection,exp}}$ are estimated to be in the range of 6.8–64.4%, 8.8–63.2%, respectively. As the flow rate increases for a given heat flux, both $(T_{heater,max} - T_{fl,in})$ and $(T_{fl,out} - T_{fluid,in})$ decrease in Eqs. (5-a) and (5-b), and both $\left(\frac{dq_{trans}}{dT_{fl,in}}\right)$ and $\left(\frac{dq_{trans}}{dT_{fl,out}}\right)$ increase in Eq. (5-c), that eventually leads to increased $\frac{U_{q_{transfer}}}{q_{transfer}}$ in Eqs. (5-a) and (5-b). In addition, as the heat flux increases for a given flow rate, both $(T_{heater,max} - T_{fl,in})$ and $(T_{fl,out} - T_{fl,in})$ increase and $\frac{U_{q_{trans}}}{q_{trans}}$ decreases in Eqs. (5-a) and (5-b). Therefore, the biggest uncertainties in $R_{total\text{-}max,exp}$ and $R_{advection,exp}$ can be found at the lowest heat flux, and the highest flow rate. The smallest uncertainties in $R_{total\text{-}max,exp}$ and $R_{advection,exp}$ can be achieved vice versa.

The uncertainty of h_{wall} is associated with each term in Eq. (3-a) and it is given as below:

$$\left(\frac{U_{h_{wall}}}{h_{wall}}\right)^2 = \left(\frac{U_{q_{trans}}}{q_{trans}}\right)^2 + \left(\frac{U_{A_{wet}}}{A_{wet}}\right)^2 + \left(\frac{U_{T_{base,avg}}}{T_{base,avg} - T_{fl,ref}}\right)^2 + \left(\frac{U_{T_{fl,ref}}}{T_{base,avg} - T_{fl,ref}}\right)^2 \quad (6)$$

The experimental uncertainties in q_{trans}, A_{wet}, $T_{base,avg}$, $T_{fl,ref}$ are 6.4–63.0%, 3.1%, 1.6–5.2%, and 1.9–2.7%, respectively. We neglected the uncertainty of η_o which was minimal to account for the uncertainty of h_{wall}. The first term in Eq. (6) is a main contributor to the uncertainty in $h_{wall,exp}$, and $U_{h_{wall,exp}}$ is estimated to be in the range of 8.1–69.9%. In addition, the uncertainty of $h_{wall,exp}$ increases as the flow rate increases because the temperature difference between $T_{base,avg}$ and $T_{fl,ref}$ decreases at a given heat flux. Lastly, the error for predicted HTC, $h_{wall,CFD}$, is due to the differences between the target u-cooler dimensions and those of the microfabricated device.

3.2.3. Uncertainty in the measured pressure drop

Since it is impossible to experimentally measure each pressure loss component from Eq. (3), the difference between the "target" μ-cooler design dimensions and "expected" fabrication variability in dimensions are considered in the uncertainty analysis of pressure drop using CFD simulations. As $\Delta P_{contraction}$ and $\Delta P_{friction}$ are two dominant components to determine ΔP_{total} (Fig. 8a), the uncertainty of $\Delta P_{contraction}$ and $\Delta P_{friction}$ are specifically analyzed:

$$\left(\frac{U_{\Delta P_{contraction}}}{\Delta P_{contraction}}\right)^2 = \left(\frac{U_{K_{contraction}}}{K_{contraction}}\right)^2 + \left(2 \cdot \frac{U_{v_{mani,in}}}{v_{mani,in}}\right)^2 \quad (7a)$$

$$\left(\frac{U_{\Delta P_{friction}}}{\Delta P_{friction}}\right)^2 = \left(\frac{U_{L_{ch}}}{L_{ch}}\right)^2 + \left(\frac{U_{D_h}}{D_h}\right)^2 + \left(\frac{U_{f_f}}{f_f}\right)^2 + \left(2 \cdot \frac{U_G}{G}\right)^2 + \left(\frac{U_{\nu_f}}{\nu_f}\right)^2 \quad (7b)$$

The error in width dimension for microchannels in cold plate/manifold is ±5 μm, and the error in height of the inlet micro-conduit and inlet plenum are ±25 μm, and ±50 μm, respectively. The errors in dimensions are observed in the actual test samples by examining the SEMs, and subsequently considered in calculation of the uncertainty in ΔP_{total} using CFD simulations. The uncertainty of $K_{contraction}$ is 21–28%, and the uncertainty of $v_{mani,in}$ is 5% (Eq. (7-a)) and the uncertainties of D_h, f_f, G are 4.6%, 9%, and 7.5%, respectively (Eq. (7-b)). With the given uncertainty values of all terms in Eqs. (7-a) and (7-b), the uncertainties of $\Delta P_{contraction}$ and $\Delta P_{friction}$ are 23–30%, and 18%, respectively.

4. Results and discussion

Water is used as the working fluid for all the experiments. We carefully established that single-phase flow and heat transfer prevails even for the highest power dissipation in this experiment, 240 W/cm^2, and lowest flow rates, 0.033 l/min, detailed in Appendix A. We organized and presented the results in the form of temperature vs. for pressure drop (Section 4.1), thermal resistance/heat transfer coefficient vs. flow rate/pressure (Section 4.2) and total pressure drop vs. flow rate (Section 4.3). For all cases, we compare the experimental data with the results of the conjugate thermal and fluid flow numerical simulations detailed in Appendix B.

4.1. Temperature rise

Fig. 6a shows the maximum and average temperature of the heater vs. pressure drop for given flow rates (0.03, 0.07 and 0.1 l/min) and heat fluxes (60, 100 and 250 W/cm^2) along with the numerical simulation results. The pressure drop across the μ-cooler is <3 kPa for all flow rates. The maximum and average temperatures of the heated surface for any given heat flux are reduced as the flow rate increases. As the heat flux increases at a constant flow rate, both maximum and average temperatures of the chip also increase. The CFD results for temperature and pressure agree well with the experimental data (Fig. 6a and b). The slight discrepancy between the measured and simulated pressures are due to potential variation in the dimensions of the microfabricated channels from the target nominal values. The associated uncertainty of heater temperature is quantified in Section 3.2.1 and is estimated to be 1.4–3.1%. The embedded microchannel-3D manifold μ-cooler device is capable of removing 250 W/cm^2 (experimental data: $T_{heater,max}$ = 90 °C) and potentially up to 850 W/cm^2 (numerical simulations: $T_{heater,max}$ = 158 °C) with only 2.3 kPa pressure drop for flow rate of 0.1 l/min, see Fig. A.I.2. We have not tested the potential maximum heat flux during the experiments because the main goal of the current work is not to check the critical heat flux of the sample, but to show minimal system pressure drop while moderate to high level heat fluxes are applied. The system pressure drop should be kept as low as possible to increase the system's coefficient of performance (COP), and the detailed information about the system pressure drop will be discussed in Section 4.3. We are planning to test higher heat fluxes with more samples in near future and try to reach up to or higher than 1 kW/cm^2 with single-phase water.

4.2. Thermal resistance and heat transfer coefficient

The q_{heater} and q_{trans} are calculated using measured applied electrical current and voltage to the serpentine heater, and the

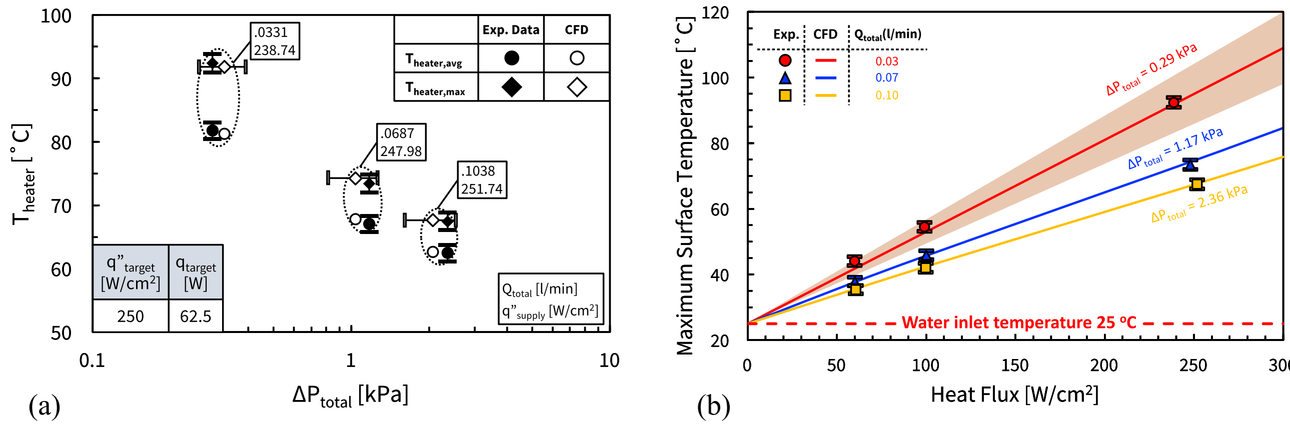

Fig. 6. The experimental data and numerical simulations results for (a) $T_{heater,max}$ or $T_{heater,avg}$ vs. ΔP_{total}, for the highest heat flux of 250 W/cm^2; dimensions of the microchannel and 3D-manifold conduits are listed in Table 1. The uncertainty in pressure drop from simulations, is mainly associated with variations of the microfabricated channel dimensions. The numerical values of the maximum and average temperatures, flow rate, pressure drop, Re number for the 9 test cases are listed in Table A.II.2, and (b) maximum surface temperature vs. heat flux for flow rates 0.03, 0.07 & 0.1 l/min. The "semi-transparent" red region, flowrate 0.03 l/min, represents ±10% uncertainty levels in CFD predictions associated with variations in μ-cooler channel and manifold conduits dimensions. (For interpretation of the references to color in this figure legend, the reader is referred to the web version of this article.)

measured change in the sensible heat of the liquid. Although we confirmed that numerical simulation indicated only 2–3% heat loss due to conduction at the periphery of the heated chip, the experimental heat loss, q_{loss}, ranged up to 19.7% of q_{heater} as the flow rate decreased. In addition, $R_{total,exp}$ became larger than $R_{total,CFD}$ as (q_{loss}/q_{heater}) increased, $R_{total,CFD}$ values were out of the error bars of $R_{total,exp}$ at the flow rate of 0.03 l/min (Fig. 7b).

The inlet temperature of the fluid, $T_{fl,in}$, is measured using a thermocouple, see Table 2. Fig. 7a depicts the measured and simulation results for $R_{total\text{-}max}$ (or $R_{total\text{-}max,exp}$) vs. flow rate for the nominal heat flux value of 250 W/cm^2, which agree well for given uncertainty levels estimated in Section 3.2.2. As expected, both $R_{total\text{-}max}$ and $R_{advection}$ decrease as the flow rate increases at a given heat flux. The convection thermal resistance, $R_{convection}$ can be estimated by $R_{convection} = R_{total-max} - R_{advection}$ and it also follows same changing trend as both $R_{total\text{-}max}$ and $R_{advection}$.

Fig. 7b shows that there is no significant change in $R_{total\text{-}max}$ as the supplied heat flux increased from 60 to 250 W/cm^2 for a given flow rate. The error bar for $R_{total\text{-}max}$ and $R_{advection}$ decreases as the flow rate increases despite of increase in the uncertainties of $R_{total\text{-}max}$ and $R_{advection}$, which is due to reduction in both $R_{total\text{-}max}$ and $R_{advection}$ along with the increase in flow rate, for details see Section 3.2.2.

Fig. 8a indicates that the heat transfer coefficient, h_{wall}, increases with flow rate. In single-phase regime, Re increases as the flow rate increases, and the thickness of thermal boundary layer is proportional to $Re^{-\frac{1}{2}}$ [25]. Therefore, h_{wall} increases as the flow rate increases due to reduction in thickness of the thermal boundary layer. The heat transfer coefficient increases weakly with the applied heat flux due to slight increase in thermal conductivity of water, see Fig. 8b. The discrepancy between the measured h_{wall} (or $h_{wall,exp}$) and CFD predictions ($h_{wall,CFD}$), is within the range of estimated uncertainty except when the flow rate was 0.03 l/min. According to Eq. (3-a), h_{wall} is linearly proportional to q_{trans} and we have confirmed that $q_{trans,exp}$ became closer to $q_{heater,exp}$ as the flow rate increased. At the flow rate of 0.03 l/min, ($q_{loss,exp}/q_{heater,exp}$) ranges from 14.9 to 19.7%, however, ($q_{loss,CFD}/q_{heater,CFD}$) is only 2–3%. As a result, $h_{wall,exp}$ became smaller than $h_{wall,CFD}$ at Q = 0.03 l/min with a given q_{supply}. Especially, the discrepancy between $h_{wall,exp}$ and $h_{wall,CFD}$ is maximized at the lowest flow rate and the heat flux, Q = 0.03 l/min, q_{supply} = 60 W/cm^2, respectively, that is detailed in Section 3.2.2.

4.3. Pressure drop

The total pressure drop, $\Delta P_{total,exp}$, across the μ-cooler device is the only directly measured quantity. The contributions of various components are evaluated using CFD simulations, Fig. 9a and b. For the highest flow rate of Q = 0.1 l/min, 34% and 5% of the total

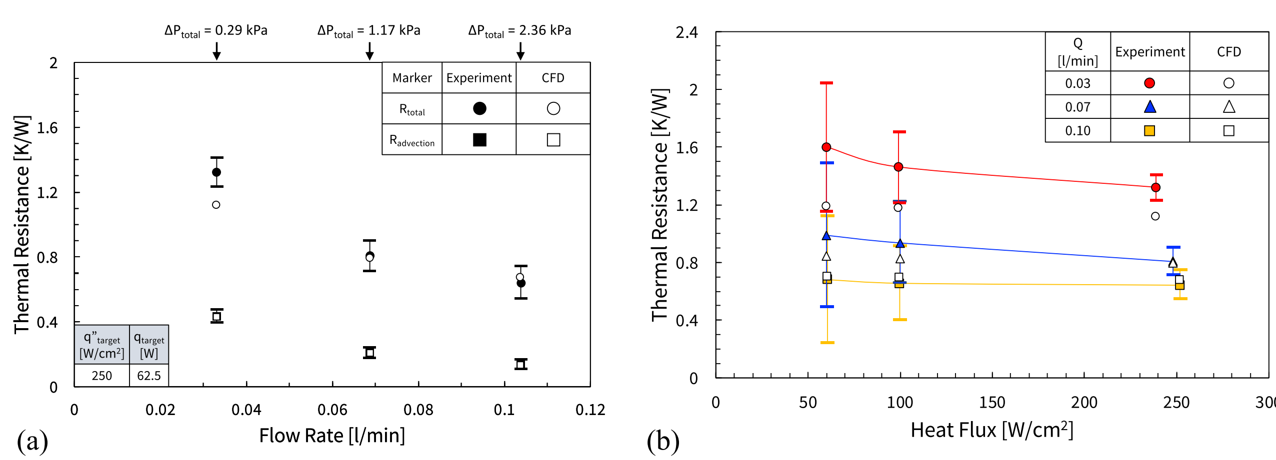

Fig. 7. Experimental data and predictions for (a) R_{total} & $R_{advection}$ vs (Flow Rate) and pressure drop for single-phase water at heat flux of 250 W/cm^2. (b) As expected, there is no significant change in R_{total} as the supplied heat flux increased from 60 to 250 W/cm^2 for a given flow rate.

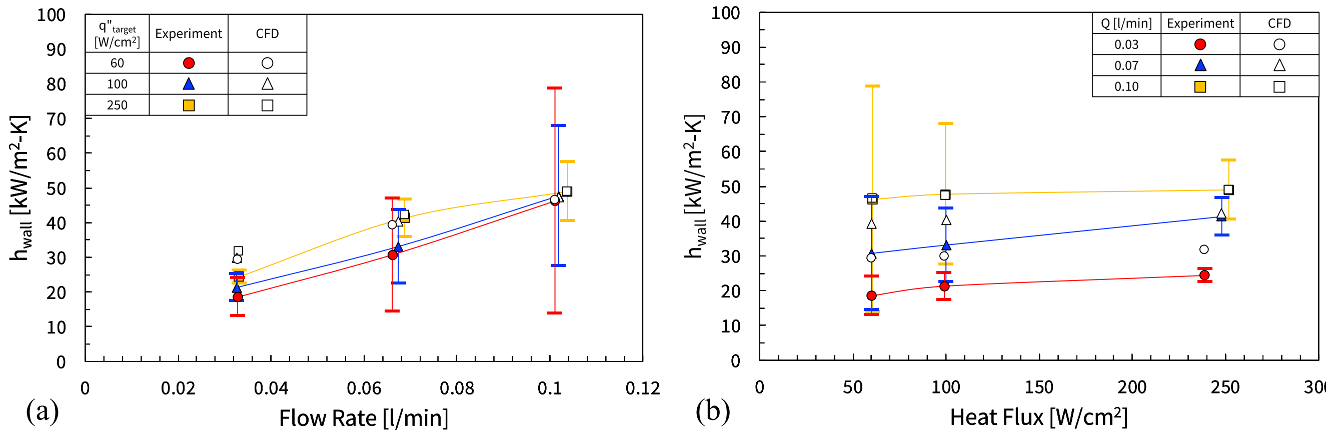

Fig. 8. The measured and simulation results for heat transfer coefficients at the cold plate microchannel walls, h_{wall}. (a) The h_{wall} vs. flow rate for various heat fluxes, and (b) the h_{wall} vs. heat flux for various flow rates.

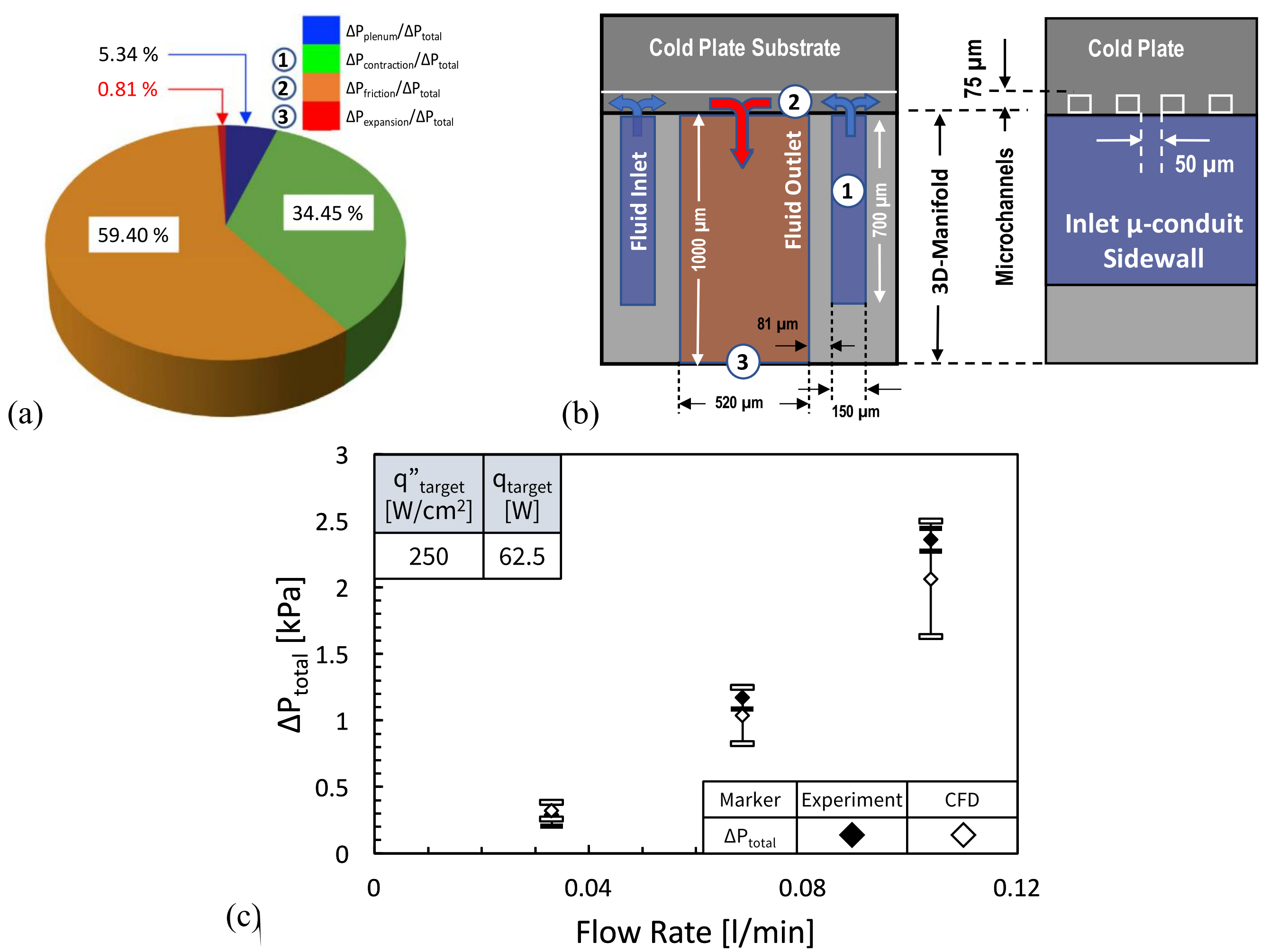

Fig. 9. Results of the CFD simulations for pressure loss in the channel and 3D manifold: (a) relative contributions of pressure drop components: ΔP_{plenum}, $\Delta P_{contraction}$, $\Delta P_{friction}$, and $\Delta P_{expansion}$ over the total pressure drop at Q = 0.1 l/min, (b) schematics of the inlet, microchannel and outlet of the µ-cooler; (c) experimental and numerical simulation results for ΔP_{total} vs Flow Rate at a nominal heat flux of q″ = 250 W/cm².

pressure drops occurs at the entrance (contraction) and exit (expansion) of microchannel to the 3D manifold conduits, respectively. Fig. 9c compares the experimental data and simulation results for pressure drop vs. flow rate, which is proportional to square of mass flux, G^2. The difference between $\Delta P_{total,CFD}$ and $\Delta P_{total,exp}$, is significantly larger than the uncertainty of the differential pressure transducer (± 0.086 kPa, see Table 2) for flow rates higher than 0.066 l/min (Fig. 9). This is due to difference between microchannel "target" design dimensions (used in numerical simulation) and that of "actual" microfabricated structure, details are discussed in Section 3.2.3. Lastly, there had been large variation in the inlet pressure as the flow rate changed. However, thermophysical property changes due to the pressure difference can be negligible compared to those by temperature changes since it is subcooled region.

5. Conclusions

We have studied the thermal performance an embedded microchannel with 3-D manifold μ-cooler heat exchanger using single-phase water as the working fluid. Design, microfabrication, test conditions, measurement process, and uncertainty analysis were discussed in detail. Conjugate numerical simulations for different test conditions were performed to predict the thermo-fluidic behavior of the designed test section. The experimental results for maximum and average temperatures of the chip, pressure drop, thermal resistance, average heat transfer coefficient for flow rates of 0.03, 0.06 and 0.1 l/min and heat fluxes of 60, 100 and 250 W/cm^2 are reported, and are in good agreement with the CFD results. The embedded microchannel-3D manifold μ-cooler device is capable of removing 250 W/cm^2 (experimental data: $T_{heater,max}$ = 90 °C) and potentially up to 850 W/cm^2 (numerical simulations: $T_{heater,max}$ = 158 °C) with only 2.6 kPa pressure drop for flow rate of 0.1 l/min, see Fig. A.I.2.

The uncertainty in calculation of the thermal resistance is particularly large due to the small temperature difference between the heater and inlet fluid, thus one should rely more on numerical simulation results. The uncertainty in predicted pressure drop, ΔP_{total} is large due to the difference between microchannel "target" design dimensions (used in numerical simulation) and that of the "actual" microfabricated structure. About 40% of the total pressure drop occurs at the entrance (contraction) and exit (expansion) of the microchannel to the 3D manifold conduits. Prior work shows that a 45° tapered entrance design significantly reduces the contraction and expansion pressure drop [23], which should be considered in future designs. Due to structural and experimental defects, some of the RTDs were not functional which prevented us from fully capturing the temperature distribution across the chip. Since then we have utilized IR thermometry for more accurate measurement of the surface temperature profile in the active region. With this improved test system, experiments employing two-phase cooling with R-245fa will be conducted for several embedded microchannel with 3D manifold μ-cooler heat exchanger designs.

Conflict of interest

The authors declare that there are no conflict of interest.

Acknowledgement

This project is supported by TOYOTA Research Institute of North America (TEMA) and the National Science Foundation Engineering Research Center for Power Optimization of Electro Thermal Systems (POETS) with cooperative agreement EEC-1449548.

Appendix A. Confirmation of single-phase flow condition

To confirm that flow and heat transfer regime remain single-phase, we evaluated the onset of nucleate boiling for the μ-cooler geometry, heat flux levels and flow conditions of the present work using the following correlation [21]:

$$\sqrt{T_{ch,base}} - \sqrt{T_{sat}} \geqslant \sqrt{2 \cdot \frac{\sigma(1+\cos\theta)}{\rho_v h_{fg}} \cdot \frac{q''_{eff}}{k_f}} \tag{7}$$

where $T_{ch,base}$ and T_{sat} are the microchannel wall temperature and liquid saturation temperature, respectively, θ is contact angle between Si and water, and q''_{eff} is effective wall heat flux on the cold-plate microchannel. For the flow rates of 0.03, 0.06 and 0.1 lit/min and at the maximum heat flux of 250 W/cm^2, we estimate the $T_{heater,max}$, $T_{ch,base}$ and $T_{f,exit}$ using the reduced order thermofluidic model detailed in [15], Fig. A.I.1(a). The estimated $T_{ch,base}$, $T_{heater,max}$, $T_{f,exit}$ and the outlet saturation temperature, T_{sat} (a function of liquid pressure) are plotted in Fig. A.I.1(b). As the flow rate increases in the closed-loop flow system, the internal pressure also increases. Therefore, P_{out} and corresponding T_{sat} are ranging from 145.38 to 231.64 kPa, from 110.43 to 124.45 °C, respectively, as the fluid flow rate increases from 0.03 to 0.1 lit/min. According to the temperature information in Fig. A.I.1(b), T_{sat} is always higher than $T_{ch,base}$ in all the experimental results, and as a matter of fact, the necessary condition for the on-set of nucleate boiling in Eq. (7) is not satisfied. Therefore, we can conclude that the fluid remained single-phase at all times.

We also utilized Eq. (7) to explore the maximum heat flux that the current embedded microchannel-3D manifold μ-cooler using single-phase water. If the predictions of Eq. (7) for the onset of boiling is accurate, the present μ-cooler can potentially remove up to 850 W/cm^2 (numerical simulations: $T_{heater,max}$ = 158 °C) with only 2.6 kPa pressure drop for flow rate of 0.1 l/min, see Fig. A.I.2.

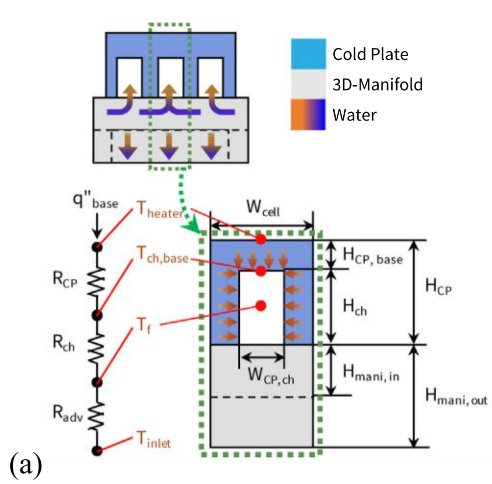

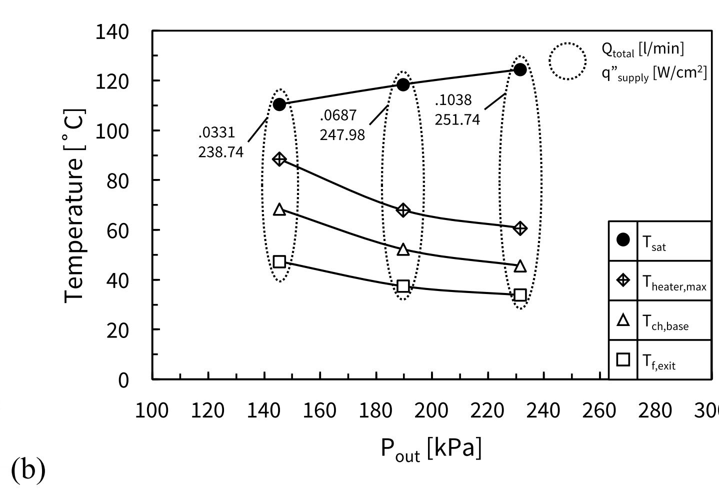

Fig. A.I.1. (a) A simplified heat conduction pathway in the embedded microchannel with 3-D manifold heat exchanger [15] and (b) Temperature vs P_{out} for single-phase water test case at the maximum heat flux 250 W/cm^2.

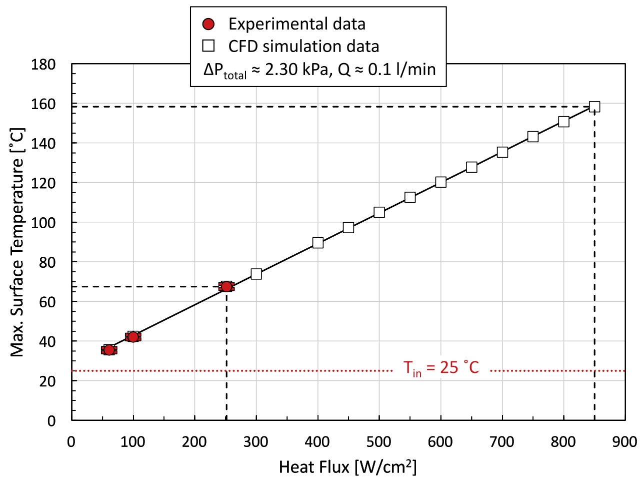

Fig. A.I.2. Experimental data and CFD modeling results for single-phase water at inlet temperature ~25 °C using a typical embedded microchannel with 3D manifold μ-cooler developed at Stanford. The experimental data are for heat flux < 250 W/cm^2. The CFD simulations are conducted to explore the feasibility of single-phase cooling at much higher heat fluxes; the onset of boiling occurs at 850 W/cm^2, to be verified experimentally. For water at inlet temperature of 25 °C, heat dissipation levels up to 500 W/cm^2 is feasible for target junction temperature of 100 °C.

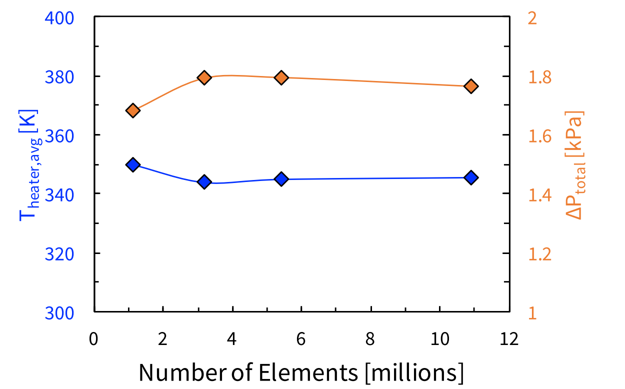

Fig. A.II.2. A study of mesh element independence at T_{in} = 293 K, Q_{in} = 0.001 kg/s, q'' = 4,494,517 W/m^2 conditions. The number of mesh elements used in the study are from 1.11E6 to 3.19E6 to 5.40E6 to 1.09E7.

Appendix B. Conjugate numerical simulation analysis

The experimental results are validated by conducting single-phase conjugate numerical simulations (ANSYS Fluent 16.0.0) for the exact μ-cooler geometry (Table 1) and flow conditions. Fig. A.II.1(a) and (b) show the solid and fluid domain for the numerical analysis, respectively. Fluid flow inlets and outlet are marked with red (↑) and blue (↓) arrows in Fig. A.II.1(b). The fluid inlet temperature is fixed at 25 °C and the inlet flow rate varies from 0.033 to 0.104 l/min. Constant heat fluxes are applied to the top surface of the Au serpentine heater which correspond to 60, 100, 250 W/cm^2 on 25 mm^2 active area. Test cases for numerical analysis are listed in Table A.II.1. Temperature-dependent thermal properties of liquid water (e.g. thermal conductivity, viscosity, density and specific heat) are considered.

A mesh size independence study is conducted with four different number of mesh elements, from 1.11E6 to 10.9E6, and the results are plotted in Fig. A.II.2. There is less than 0.31% change in the average heater temperature, $T_{heater,avg}$, and 1.7% change in the total pressure drop, ΔP_{total}, if the number of mesh element is higher than 3.19E6. Therefore, the number of mesh element used in this study was 5.39E6 based on the mesh independence study.

Numerical simulations are conducted for the test cases 1–9 outlined in Table A.II.1, the results for total pressure drop, maximum and average heater temperatures, fluid outlet temperature, total thermal resistance of the μ-cooler and the Reynolds numbers are given in the Table A.II.2.

As noted in Section 2.1, due to microfabrication defects only four RTD5, 6, 7, and 9 were functional (see Fig. 2a). Therefore, the calculated average surface temperature using these four RTDs,

Table A.II.1
Test matrix for the numerical analysis.

Test #	Heat flux [W/cm^2]	Supplied heat [W]	Mass flow rate [kg/s]
1	60	15	5.450E−4
2			1.098E−3
3			1.680E−3
4	100	25	5.420E−4
5			1.120E−3
6			1.693E−3
7	238.74	59.69	5.500E−4
8	250	62.50	1.142E−3
9	250	62.50	1.725E−3

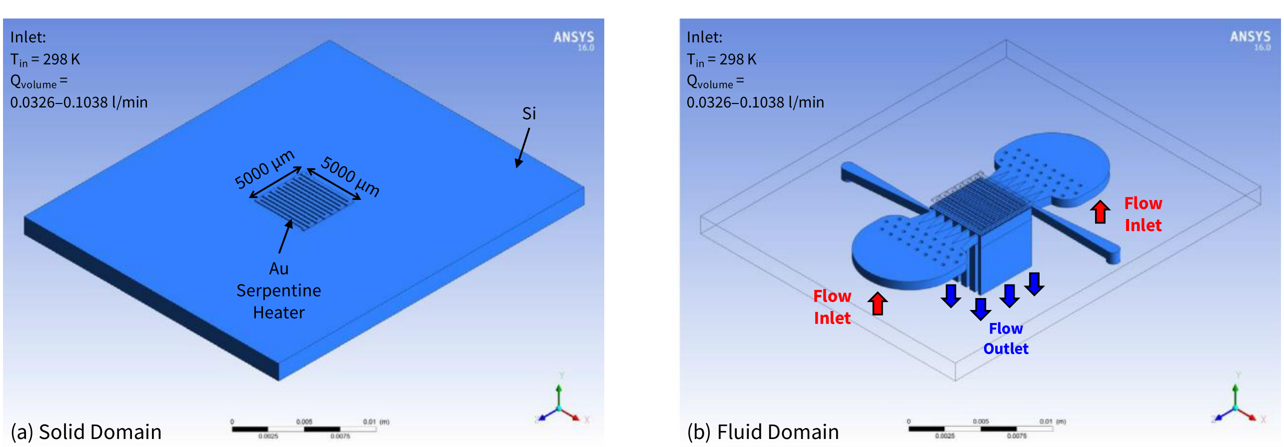

Fig. A.II.1. (a) Solid and (b) fluid domains for the conjugate numerical analysis.

Table A.II.2
Numerically predicted thermo-fluidic information in all test cases.

Test number	ΔP_{total} [kPa]	$T_{heater,\ max}$ [°C]	$T_{heater,avg\text{-}global}$ [°C]	$T_{out,\ avg}$ [°C]	$f_1 = T_{heater,avg\text{-}global}/T_{heater,avg\text{-}local}$	$f_2 = T_{heater,max}/T_{heater,avg\text{-}local}$	R_{total} [K/W]	Re_{max}
1	0.3679	42.78	39.78	31.51	1.0604	1.1404	1.1869	40.10
2	1.0321	37.68	35.90	28.27	1.0546	1.1069	0.8453	76.06
3	2.0377	35.66	34.36	27.16	1.0520	1.0919	0.7041	113.14
4	0.3522	54.09	49.25	35.80	1.0815	1.1877	1.1745	41.59
5	1.0496	45.70	42.86	30.33	1.0768	1.1482	0.8285	78.78
6	2.0491	42.39	40.29	28.52	1.0742	1.1303	0.6974	115.10
7	0.3237	91.82	81.26	50.59	1.1184	1.2638	1.1195	47.07
8	1.0389	74.28	67.84	37.93	1.1219	1.2282	0.7948	85.29
9	2.0649	67.63	62.63	33.73	1.1240	1.2138	0.6774	121.53

$T_{heater,avg\text{-}local}$, is not a precise representation of the average temperature over the entire surface of the heater, $T_{heater,avg\text{-}global}$. The scaling factors f_1 and f_2, are calculated using CFD simulations, represent the ratios between $T_{heater,avg\text{-}local}$ to $T_{heater,avg\text{-}global}$, $T_{heater,max}$, respectively, and are given columns 6 and 7 of Table A.II.2.

References

[1] Electrical and electronics technical team roadmap, Electrical and Electronics Technical Team, U.S. Dept. of Energy, Washington, DC, 2006.
[2] A. Bar-Cohen, Gen-3 thermal management technology: role of microchannels and nanostructures in an embedded cooling paradigm, J. Nanotechnol. Eng. Med. 4 (2) (2013).
[3] D.B. Tuckerman, R.F.W. Pease, High-performance heat sinking for VLSI, IEEE Electron. Device Lett. 2 (5) (1981) 126–129.
[4] G.M. Harpole, J.E. Eninger, Micro-channel heat exchanger optimization, in: 7th IEEE SEMI-THERM Symposium, 1991, pp. 59–63.
[5] J.H. Ryu, D.H. Choi, S.J. Kim, Three-dimensional numerical optimization of a manifold microchannel heat sink, Int. J. Heat Mass Transf. 46 (9) (2003) 1553–1562.
[6] Y.H. Kim, W.C. Chun, J.T. Kim, B.C. Pak, B.J. Baek, Forced air cooling by using manifold microchannel heat sinks, J. Mech. Sci. Technol. 12 (4) (1998) 709–718.
[7] E. Kermani, S. Dessiatoun, A. Shooshtari, M.M. Ohadi, Experimental investigation of heat transfer performance of a manifold microchannel heat sink for cooling of concentrated solar cells, in: Electronic Components and Technology Conference, San Diego, USA, 2009, pp. 453–459.
[8] L. Boteler, N. Jankowski, P. McCluskey, B. Morgan, Numerical investigation and sensitivity analysis of manifold microchannel coolers, Int. J. Heat Mass Transf. 55 (25–26) (2012) 7698–7708.
[9] M.A. Arie, A.H. Shooshtari, S.V. Dessiatoun, M.M. Ohadi, E. Al-Hajri, Simulation and thermal optimization of a manifold microchannel flat plate heat exchanger, in: ASME 2012 International Mechanical Engineering Congress and Exposition, American Society of Mechanical Engineers, 2012, pp. 209–220.
[10] M.A. Arie, A. Shooshtari, S. Dessiatoun, M.M. Ohadi, Thermal optimization of an air-cooling heat exchanger utilizing manifold-microchannels, in: IEEE Intersociety Conference on Thermal and Thermomechanical Phenomena in Electronic Systems (ITherm), 27–30 May, 2014, 2014, pp. 807–815.
[11] M.A. Arie, A.H. Shooshtari, S.V. Dessiatoun, E. Al-Hajri, M.M. Ohadi, Numerical modeling and thermal optimization of a single-phase flow manifold microchannel plate heat exchanger, Int. J. Heat Mass Transf. 81 (2015) 478–489.
[12] S. Sarangi, K.K. Bodla, S.V. Garimella, J.Y. Murthy, Manifold microchannel heat sink design using optimization under uncertainty, Int. J. Heat Mass Transf. 69 (2014) 92–105.
[13] F. Zhou, Y. Liu, Y. Liu, S.N. Joshi, E.M. Dede, Modular design for a single-phase manifold mini/microchannel cold plate, J. Therm. Sci. Eng. Appl. 8 (2016) 021010.
[14] E. Cetegen, Force Fed Microchannel High Heat Flux Cooling Utilizing Microgrooved Surfaces, University of Maryland, College Park, 2010, Ph.D..
[15] M.M. Ohadi, K. Choo, S. Dessiatoun, E. Cetegen, Next Generation Microchannel Heat Exchangers, Springer Publishing Co., 2012.
[16] D.G. Bae, R.K. Mandel, S.V. Dessiatoun, S. Rajgopal, S.P. Roberts, M. Mehregany, M.M. Ohadi, Embedded two-phase cooling of high heat flux electronics on silicon carbide (SiC) using thin-film evaporation and an enhanced delivery system (FEEDS) manifold-microchannel cooler, in: IEEE ITHERM Conference, 29 May–1 June, 2017, 2017, pp. 466–472.
[17] R.K. Mandel, D.G. Bae, M.M. Ohadi, Embedded two-phase cooling of high flux electronics via press-fit and bonded FEEDS coolers, J. Electron. Packag. 140 (3) (2018) 031003.
[18] K.P. Drummond, J.A. Weibel, S.V. Garimella, D. Back, D.B. Janes, M.D. Sinanis, D. Peroulis, Evaporative intrachip hotspot cooling with a hierarchical manifold microchannel heat sink array, in: IEEE ITHERM Conference, 31 May – 3 June, 2016, 2016, pp. 307–315.
[19] K.P. Drummond, D. Back, M.D. Sinanis, D.B. Janes, D. Peroulis, J.A. Weibel, S.V. Garimella, Characterization of hierarchical manifold microchannel heat sink arrays under simultaneous background and hotspot heating conditions, Int. J. Heat Mass Transf. 126 (2018) 1289–1301.
[20] K.W. Jung, C.R. Kharangate, H. Lee, J. Palko, F. Zhou, M. Asheghi, E.M. Dede, K.E. Goodson, Microchannel cooling strategies for high heat flux (1 kW/cm^2) power electronic applications, in: IEEE ITHERM Conference on Thermal and Thermomechanical Phenomena in Electronic Systems (ITherm), 29 May–1 June, 2017, 2017, pp. 98–105.
[21] D. Liu, P.-S. Lee, S.V. Garimella, Prediction of the onset of nucleate boiling in microchannel flow, Int. J. Heat Mass Transf. 48 (2005) 5134–5149.
[22] E. Jing, B. Xiong, Y. Wang, Low-temperature Au-Si water bonding, J. Micromech. Microeng. 20 (2010) 095015.
[23] H. Lee, Y. Won, F. Houshmand, C. Gorle, M. Asheghi, K.E. Goodson, Computational modeling of extreme heat flux microcooler for GaN-based HEMT, ASME International Technical Conference and Exhibition on Packaging and Integration of Electronic and Photonic Microsystems (InterPACK), July 6 - July 9, San Francisco, 2015.
[24] S.J. Kline, F.A. McClintock, Describing Uncertainties in Single-Sample Experiments, Mech. Eng., January 1953, p. 3.
[25] F.P. Incropera, Fundamentals of Heat and Mass Transfer, John Wiley & Sons, 2011.